

Deep crustal heating for realistic compositions of thermonuclear ashes

N.N. Shchepochin,^{*} M.E. Gusakov, A.I. Chugunov

Ioffe Institute, Polytekhnicheskaya 26, 194021 Saint Petersburg, Russia

Accepted 2021 xxxx. Received 2021 xxxx; in original form 2021 xxxx

ABSTRACT

The deep crustal heating, associated with exothermal nuclear reactions, is believed to be a key parameter for describing the thermal evolution of accreting neutron stars. In this paper, we present the first thermodynamically consistent calculations of the crustal heating for realistic compositions of thermonuclear ashes. In contrast to previous studies based on the traditional approach, we account for neutron hydrostatic/diffusion (nHD) equilibrium condition imposed by superfluidity of neutrons in a major part of the inner crust and rapid diffusion in the remaining part of the inner crust. We apply a simplified reaction network to model nuclear evolution of various multi-component thermonuclear burning ashes (superburst, KEPLER, and extreme rp-process ashes) in the outer crust and calculate the deep crustal heating energy release Q , parametrized by the pressure at the outer-inner crust interface, P_{oi} . Using the general thermodynamic arguments, we set a lower limit on Q , $Q \gtrsim 0.13 - 0.2$ MeV per baryon (an actual value depends on the ash composition and the employed mass model).

Key words: stars: neutron, accretion discs, X-rays: binaries

1 INTRODUCTION

In neutron star (NS) low-mass X-ray binaries (LMXBs) a mass transfer from a less compact donor star (typically, with the mass $\lesssim M_{\odot}$) via Roche-lobe overflow triggers numerous observable phenomena. One of them is the thermonuclear burning of light elements on the NS surface. Depending on accreted matter composition and accretion rate, burning proceeds in different regimes (Johnston 2020) and produces ashes, consisting of large number of heavy nuclei (see, e.g., Schatz et al. 2001; Keek & Heger 2011; Cyburt et al. 2016). Afterwards, the newly-fallen material pushes the ashes inward the star, so that their compression induces exothermic nuclear reactions (Sato 1979; Haensel & Zdunik 1990a; Gusakov & Chugunov 2020). These reactions heat up the NS crust, leading to the observable thermal emission in quiescent periods between the accretion episodes (Brown, Bildsten & Rutledge 1998; Levenfish & Haensel 2007; Heinke et al. 2009; Potekhin, Chugunov & Chabrier 2019; Parikh et al. 2021a; Parikh et al. 2021b).

Comparison of the NS crust cooling curves to the theoretical models of heat relaxation (Rutledge et al. 2002; Shternin et al. 2007; Brown & Cumming 2009; Cackett et al. 2010; Page & Reddy 2013; Degenaar, Wijnands & Miller 2013; Meisel et al. 2018; Parikh et al. 2019; Wijngaarden et al. 2020; Potekhin & Chabrier 2021), as well as modelling of the steady-state thermal configurations (Brown et al. 1998; Yakovlev, Levenfish & Haensel 2003; Yakovlev et al. 2004;

Heinke et al. 2007, 2009; Wijnands, Degenaar & Page 2013; Beznogov & Yakovlev 2015; Han & Steiner 2017; Fortin et al. 2018; Brown et al. 2018; Potekhin et al. 2019; Fortin et al. 2021) allows one to constrain the properties of NS matter. To model the thermal evolution one needs to know the profile of energy release, the crust equation of state (EOS) and composition, which can be found by studying the chain of nuclear reactions in the crust of an accreting NS.

First calculations of the accreted crust structure were performed by Sato (1979). Later, Haensel & Zdunik (1990a,b, 2003, 2008) constructed a set of the most widely-used models, based on the compressible liquid-drop model (CLD) of Mackie & Baym (1977). These models were recently updated by Fantina et al. (2018), who implemented realistic Skyrme-type parametrization of nucleon interactions suggested by Goriely et al. (2010) and work within the semiclassical extended Thomas-Fermi approach (see, e.g., Brack et al. 1985) with shell corrections included ‘on top’ by Strutinsky (1967) integral theorem. These studies adopted a one-component approximation, assuming that nuclei of only one type exist at any given pressure. Gupta et al. (2007, 2008) and Steiner (2012) went beyond the one-component approximation. Recently, Lau et al. (2018) presented detailed calculations of the crust composition and heat release down to the depth in the inner crust with the density $\rho \lesssim 2 \times 10^{12}$ g cm⁻³. They used full reaction network and realistic compositions of nuclear ashes. Finally, Shchepochin & Chugunov (2019) investigated the dependence of the crust parameters on the employed mass model using the simplified reaction network and found a rea-

^{*} nicknicklas@mail.ru

sonable agreement with the results of [Lau et al. \(2018\)](#) for initial ^{56}Fe composition, if the same mass model is applied.

All the papers quoted above consider nuclear reactions in a compressing matter element, keeping the number of baryons in this element fixed during the compression (the traditional approach). Inconsistency of the traditional approach was pointed out by [Chugunov & Shchechilin \(2020\)](#): it neglects possible redistribution of unbound neutrons in the inner crust. The way out was suggested by [Gusakov & Chugunov \(2020\)](#), who developed a thermodynamically consistent approach, that accounts for redistribution of neutrons. The approach rests on the neutron Hydrostatic and Diffusion (nHD) equilibrium condition in the inner crust, $\mu_n^\infty = \mu_n e^{\nu/2} = \text{const}$, where μ_n is the (local) neutron chemical potential, and $e^{\nu/2}$ is the redshift factor. In the major part of the inner crust this condition should hold in order for the superfluid neutrons there to be in hydrostatic equilibrium; in turn, in the remaining nonsuperfluid region the condition is satisfied due to the efficient neutron diffusion ([Gusakov & Chugunov 2020](#)).

Modelling of the accreted crust within the nHD approach appears to be much more intricate than in the traditional approach, because one should self-consistently study nuclear reactions in the whole inner crust, accounting for, simultaneously, the nHD and general hydrostatic equilibrium conditions. To do so one should treat the pressure P_{oi} at the outer-inner (oi) crust interface as a parameter, which, generally, does not coincide with the neutron-drip pressure, but varies during the accretion process as EOS itself, until the fully accreted (FA) crust is established ([Gusakov & Chugunov 2020](#)). For FA crust, the nuclear reactions proceed in the regime, which keeps the crust EOS without noticeable changes. In particular, the total number of nuclei in the crust is conserved (up to a small secular variation associated with the increasing NS mass).

To keep the number of nuclei in the crust fixed, an efficient mechanism of nuclei disintegration is required. Such mechanism indeed exists in the form of a specific instability, which typically occurs in the bottom layers of the inner crust (see [Gusakov & Chugunov 2020](#) for details). As discussed in [Gusakov & Chugunov \(2021\)](#) (GC21 in what follows), the instability is affected by the nuclear shell effects. Furthermore, part of the crust can be located below the instability, being decoupled from the rest of the crust (i.e., newly accreted nuclei do not reach this region). The composition of this part of the crust is determined during accretion before the crust becomes fully accreted. Because of these difficulties, accurate prediction of the FA crust EOS within the thermodynamically consistent approach stays an open problem.

However, as shown in GC21, the details of nuclear evolution in the inner crust are not so important, if one is only interested in the total deep crustal heating energy release Q (see section 3.2 for the accurate definition, which takes into account the redshift factors). Namely, Q can be calculated by modelling the outer crust EOS at $P < P_{oi}$, where pressure P_{oi} is treated as a free parameter, which encodes all information on the reactions in the inner crust, including the nuclei disintegration process (GC21). This allows one to separate the problem of Q determination into two steps: in the first step Q is calculated as a function of P_{oi} and in the second step the value of P_{oi} is determined by accurate modelling of the crust evolution in the course of accretion. In this paper,

we consider only the first step, leaving the second one for the subsequent work.

The paper is organized as follows. In section 2 we describe the simplified reaction network applied to studying the nuclear evolution in the outer crust. In section 3.1 we present results of this modelling for various initial compositions of the ashes and nuclear mass models, in particular, we calculate the heat release in the outer crust, Q_o . In section 3.2 we calculate the heat release below the outer crust, Q_{inner} , and the net deep crustal heating energy release, Q . The quantities Q_o , Q_{inner} and Q are parametrized by the pressure P_{oi} . Additionally, in Appendix A we present profiles of the average charge and impurity parameter in the outer crust for all the considered models.

2 SIMPLIFIED REACTION NETWORK IN THE OUTER CRUST

In the outer crust, the pressure is almost completely determined by the degenerate relativistic electrons, i.e., the pressure growth is associated with the increasing electron chemical potential μ_e . Increase of μ_e induces electron captures by nuclei (typically, the captures occur in a pairwise fashion due to even-odd staggering, see, e.g., [Haensel & Zdunik 1990a](#)). For the considered compositions of nuclear ashes some nuclei become very neutron-rich at the bottom layers of the outer crust, so that they emit neutrons after electron captures. However, the total amount of the emitted neutrons is very small. Because neutron diffusion timescale is typically much larger than the characteristic time of neutron absorptions, we assume, that neutrons are captured by other nuclei, located at the same depth (a probability to adsorb neutron during the neutron-nuclear scattering is not small enough to allow for a large number of scattering events, required for neutron diffusion over any reasonable distance). Another consequence of electron captures is the appearance of elements with a low proton number Z , for which pycnonuclear fusion reactions appear to be possible ([Yakovlev et al. 2006](#)). In some cases, in a complex chain of reactions, the emission of electrons turns out to be energetically favourable. Consequently, in the outer crust one should consider electron emissions/captures, neutron emissions/captures, and pycnonuclear fusions (for simplicity, in this work we neglect neutron transfer reactions, considered by [Saakyan & Avakyan 1972](#); [Chugunov 2019](#)).

2.1 Reaction network

Let us briefly remind the main points of the simplified reaction network discussed in [Shchechilin & Chugunov \(2019\)](#) and applied here. The approach, generally, follows that of [Steiner \(2012\)](#), and is based on the minimization of the Gibbs energy at constant pressure, neglecting thermal corrections. We start with some initial pressure P_{in} and gradually increase it, step by step, mimicking compression of a given matter element in the outer crust. At each compression step, we check for available reactions that can decrease the Gibbs energy. If some reaction is open, we accurately adjust the pressure to the reaction's threshold value. In this way, we avoid unphysical energy release associated with the stepwise increase of the pressure. After the first reaction occurred, the subsequent admissible reactions (if any) proceed at constant pressure

by small chunks until none of the reactions are energetically favourable. Then we decide that the matter composition at this P is established and we can further increase the pressure.

In our simplified reaction network the order of the reaction chunks is controlled by the following priority rules: (a) neutron emission, (b) neutron capture, (c) electron emission/capture plus (optional) neutron emission, (d) neutron capture and electron emission/capture, (e) capture of 2 neutrons, (f) pycnonuclear fusion. Among the allowed reactions of the same type, the most energetically favourable reaction goes first. These priority rules are based on the estimates of the reaction rates (Shchechilin & Chugunov 2019) with few modifications. First, following Fantina et al. (2018) we now allow for the electron emissions/captures accompanied by neutron emissions/captures [reaction types (c) and (d)]. Second, the priority of the two-neutron-capture reaction is reduced. As discussed in Shchechilin & Chugunov (2019), this reaction was included into the simplified reaction network to mimic two successive neutron captures in the inner crust, if the first one is not energetically favourable, but proceeds in the (more realistic) detailed network due to thermal activation. Here we apply our network to the outer crust, where a very small amount of unbound neutrons is expected (see, e.g., figure 7 in Lau et al. 2018) and it seems unnecessary to consider two-neutron-captures, but the analysis of the reaction pathways shown in Lau et al. (2018) reveals that this process takes place in their network. To include this possibility, we retain the reaction type (e) in our network, but with reduced priority. In numerical simulations the reaction (e) allows to absorb unbound neutrons, released by reactions (a) and (c), if one-neutron-capture reaction is forbidden.

In our model the fusion reactions are only allowed if the respective timescale does not exceed the accretion time (i.e., the replacement time $\tau \approx P/(g\dot{m}_{\text{fid}})$ for an accreted layer with the pressure P , where the fiducial accretion rate is taken to be $\dot{m}_{\text{fid}} = 0.3\dot{m}_{\text{Edd}}$; $\dot{m}_{\text{Edd}} = 8.8 \times 10^4 \text{ g cm}^{-2} \text{ s}^{-1}$ is the Eddington accretion rate, and $g = 1.85 \times 10^{14} \text{ cm s}^{-2}$ is the gravitational acceleration). To estimate the reaction timescale we apply the thermally enhanced pycnonuclear reaction rates from Yakovlev et al. (2006) with S -factors from Afanasjev et al. (2012). As in Lau et al. (2018), the temperature is assumed to be fixed, $T = 5 \times 10^8 \text{ K}$. Our reaction network depends on the temperature only via the fusion reaction rates.

Following Haensel & Zdunik (2008) and Fantina et al. (2018), we completely neglect neutrino losses when calculating the energy release for all nuclear reactions (this is justified by the work of Gupta et al. (2007), where excited states are taken into account). In Shchechilin & Chugunov (2019) we demonstrate that the simplified reaction network is in a reasonable agreement with the results of detailed network of Lau et al. (2018) for pure ^{56}Fe composition of nuclear ashes (see also Fig. A3 in Appendix A and section 3.3 in Gupta et al. 2007 for a discussion of applicability of approximate models).

2.2 Physics input

To implement the simplified reaction network, one should specify the model for calculating the Gibbs energy for a given nuclear composition. The physics of plasma in the outer crust of accreting neutron stars is rather well-known (see, e.g., Haensel et al. 2007; here we apply the same model as in Shchechilin & Chugunov 2019) so that the masses of nuclei

become the main source of uncertainty. If available, we use experimental results from the Atomic Mass Evaluation 2020 (AME20; Wang et al. 2021).¹ For comparison, the results based on the previous version of the atomic mass evaluation (AME16, Wang et al. 2017) are shown in Figs. B2 and B3 in Appendix B, and also discussed in depth in the first arXiv version of this paper.²

However, in the bottom regions of the outer crust we also need to use the theoretical mass models. Despite the fact that the modern mass models agree well with the experimental data (rms deviation is about 0.6 MeV), the mass difference between particular elements can reach $\sim 10 \text{ MeV}$ (see Fig. B1 in Appendix B). To check the degree of model independence of our results, we apply several theoretical atomic mass tables, namely, two finite-range droplet models, FRDM92 Möller et al. (1995) and FRDM12 Möller et al. (2016), together with the Hartree-Fock-Bogoliubov model HFB24 from Goriely et al. (2013).³ To obtain the masses of nuclei, the electron rest mass and binding energy $E_{e,b}$ is subtracted using the fitting formula $E_{e,b} = 14.33Z^{2.39} \text{ eV}$ (see Lunney et al. 2003) for all mass tables. In our calculations, we use the mass tables obtained by combining AME20 with the respective theoretical mass tables (the ‘joint’ approach; see Shchechilin & Chugunov 2019 for details and discussion of mass table merging). For simplicity, we include only ground state to ground state transitions, that allow us to avoid uncertainty related to the structure of excited states.

2.3 Initial composition and numerical implementation

The thermonuclear burning in the shallow crust regions can occur in different regimes, leading to various ash compositions (Johnston 2020). Following Lau et al. (2018), we consider three representative models of nuclear ashes: extreme rapid proton capture (extreme rp-process) ashes (Schatz et al. 2001), KEPLER X-ray burst ashes (Cyburt et al. 2016), and superburst ashes (Cumming et al. 2006). The corresponding ash compositions are extracted from figures 9, 15, 18 of Lau et al. (2018). Note that, the most abundant elements in the superburst and KEPLER ashes are from the same group of elements with the mass number $A \approx 60$ (^{56}Fe and ^{64}Ni for superburst and KEPLER ashes, respectively). In turn, for extreme rp-process ashes the abundance peak is shifted to $A = 106$ (and is dominated by ^{106}Ru), due to efficient generation of heavy elements by rapid proton captures.

For numerical simulations we take 500 nuclei, thereby the abundances from Lau et al. (2018) are rounded; we checked that this choice does not affect our conclusions.⁴ The charge

¹ The table for AME20 is downloaded from <https://www-nds.iaea.org/amdc/>. Extrapolated mass values from this table are ignored.

² <https://arxiv.org/pdf/2105.01991v1.pdf>

³ The tables for FRDM92, FRDM12 and HFB24 models are downloaded from <http://t2.lanl.gov/nis/molleretal/publications/ADNDT-59-1995-185-files.html>, <http://t2.lanl.gov/nis/molleretal/publications/ADNDT-FRDM2012.html>, and <http://www.astro.ulb.ac.be/bruslib/nucdata/hfb24-dat> (Xu, Y. et al. 2013), respectively.

⁴ We use two independent codes, with a bit different realization of the minimization procedure. Both codes give similar results.

number Z for each A in the ashes is chosen to be the most bound nuclei in the terrestrial conditions ($P = 0$). Then, rising the pressure to $P_{\text{in}} = 6 \times 10^{26} \text{ dyn cm}^{-2}$ we obtain the initial set of nuclei to start our simulations. The reaction network can be used as described in Sec. 2.1 up to the outer-inner crust interface, corresponding to the pressure P_{oi} and should be modified in the inner crust to take into account the nHD condition.

As shown in GC21, the pressure P_{oi} depends on the (still) rather uncertain nuclear shell effects in the deep layers of the inner crust; it can also depend on the accretion history. Thus, here we treat P_{oi} as a free parameter of the outer crust models, leaving construction of the inner crust models and accurate determination of P_{oi} as a task for the future.

Note that there is no need for recalculating the outer crust model for each given pressure P_{oi} . Instead, it is instructive to proceed as follows. As a first step, we generate the traditional model of the outer crust by running our simplified reaction network up to the neutron drip pressure $P_{\text{nd}}^{(\text{acc})}$, which is rigorously defined in the traditional approach (it is the minimum pressure at which unbound neutrons appear in the accreted crust and are not captured by nuclei, assuming that the nHD condition is ignored; Haensel & Zdunik 1990a, 2003, 2008; Steiner 2012; Lau et al. 2018; Shchechilin & Chugunov 2019). The obtained *traditional* outer-crust model does not have a direct physical meaning as long as $P_{\text{oi}} < P_{\text{nd}}^{(\text{acc})}$, but it will be helpful in the second step. Namely, at the second step, we specify P_{oi} and produce the realistic outer-crust model by cutting off the $P > P_{\text{oi}}$ part of the traditional model generated at the first step.

By construction, this two-step procedure is applicable if $P_{\text{oi}} < P_{\text{nd}}^{(\text{acc})}$; the latter condition agrees with the numerical results of (Gusakov & Chugunov 2020, GC21), which are obtained assuming pure ^{56}Fe ash composition. However, we should warn the reader, that we are not aware of a rigorous proof that P_{oi} can never exceed $P_{\text{nd}}^{(\text{acc})}$. If, for some specific conditions (e.g., ash composition and/or inner-crust nuclear-physics model), P_{oi} will appear to be larger than $P_{\text{nd}}^{(\text{acc})}$, the outer crust model at $P > P_{\text{nd}}^{(\text{acc})}$ should be supplemented to account for *sedimentation* of unbound neutrons into the inner crust. We leave a detailed analysis of this (rather exotic) possibility beyond the scope of the present work.

3 RESULTS

3.1 Nuclear evolution and heat release in the outer crust

We calculate the nuclear composition in the outer crust by applying AME20 for nuclei with experimentally known masses and one of the theoretical nuclear mass models (FRDM92, FRDM12, and HFB24) otherwise (see section 2.2). In Fig. 1 we show the heat release in the outer crust, $Q_{\text{o}}(P_{\text{oi}})$. For simplicity, as in all the previous works (e.g., Haensel & Zdunik 2008; Lau et al. 2018; Fantina et al. 2018), we neglect variation of the redshift factor in the outer crust and calculate $Q_{\text{o}}(P_{\text{oi}})$ as a (simple) sum over the heat sources located at pressures lower than P_{oi} . Two curves for HFB24 mass model terminate at $P_{\text{oi}} = P_{\text{nd}}^{(\text{acc})}$ (for most of the models $P_{\text{nd}}^{(\text{acc})}$ is larger than $10^{30} \text{ dyn cm}^{-2}$, the maximum pressure shown in Fig. 1).

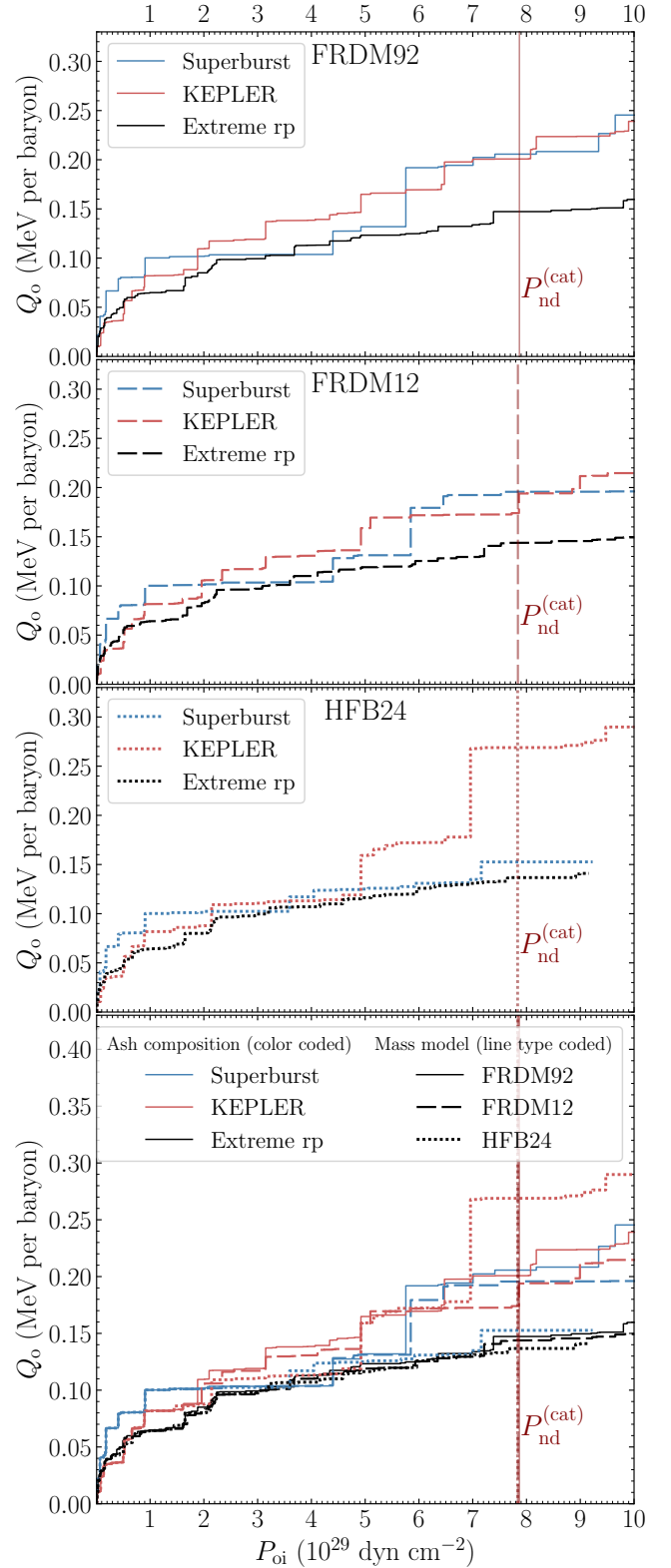


Figure 1. Q_{o} vs P_{oi} for the three ash compositions considered in the paper. Three upper panels correspond to the three mass models (from the top: FRDM92, FRDM12, and HFB24), the bottom panel shows all the plots in one figure. Ash composition is colour coded: superburst – blue; KEPLER – red; extreme rp – black; mass model is line type coded: FRDM92 – solid; FRDM12 – dashed; HFB24 – dotted. The vertical lines represent the pressure $P_{\text{nd}}^{(\text{cat})}$ at the oi interface for the cold catalysed matter (line type corresponds to the mass model).

It is worth stressing, that the heat release profile for $P < P_{oi}$ is not affected by the nHD condition. As a result, the integrated heat release up to a given pressure P can be easily read out from Fig. 1 as $Q_o(P)$. Conversely, it allows one to map previously calculated heat release profiles (e.g., Haensel & Zdunik 1990a, 2003, 2008; Steiner 2012; Lau et al. 2018; Fantina et al. 2018; Shchepochin & Chugunov 2019; Chamel et al. 2020) to obtain $Q_o(P_{oi})$ dependence for these models.

Up to the pressure $\lesssim 5 \times 10^{28} \text{ dyn cm}^{-2}$ the crust is mostly composed of nuclei with experimentally measured masses and the nuclear reaction chain is almost independent of the theoretical mass model (see bottom panel in Fig. 1). To extend the calculation to higher pressures theoretical mass tables are required and, as a consequence, $Q_o(P_{oi})$ curves start branching, indicating sensitivity of the results to the employed mass model. For instance, for superburst ashes Q_o predicted by HFB24 and FRDM92 mass models can differ by a factor of 1.3 for $P_{oi} \approx 8 \times 10^{29} \text{ dyn cm}^{-2}$ (about 0.05 MeV per accreted baryon). This difference is mainly associated with the model-dependent Q -values of nuclear reactions. In this case, the predominant contribution comes from the reaction $^{56}\text{Ca}(2e^-, 2\nu_e)^{56}\text{Ar}$. For FRDM92 mass model the second electron capture gives 6.37 MeV (per nucleus), whereas for HFB24 mass model only 0.71 MeV is released (the difference in the masses of ^{56}K and ^{56}Ar for two models is visible in the mass charts of Fig. B1). On the contrary, for the extreme rp-process ashes all applied mass models predict almost the same $Q_o(P_{oi})$ dependence. For FRDM12 and FRDM92 mass models heating profiles for superburst and KEPLER ashes become rather similar (see first two panels in Fig. 1).

For all the considered mass models and $P_{oi} \gtrsim 10^{29} \text{ dyn cm}^{-2}$, extreme rp-process ashes lead to the lowest $Q_o(P_{oi})$ among all studied ash compositions. Taking $P_{oi} = P_{nd}^{(cat)}$, the heat release in the outer crust can be estimated as $Q_o \sim (0.14 - 0.15) \text{ MeV}$ per accreted baryon for mixtures of elements with abundance peak at $A = 106$, and $Q_o \sim (0.15 - 0.27) \text{ MeV}$ in the case $A \approx 60$. Quite similar values can be obtained by using the heat release profiles from the one-component model of Haensel & Zdunik (2008) or Fantina et al. (2018) ($Q_o \sim 0.13 \text{ MeV}$ for ashes composed of ^{106}Pd , and $Q_o \sim (0.13 - 0.20) \text{ MeV}$ for ^{56}Fe , all per accreted baryon; see also GC21).

At the same time, somewhat higher values are presented by Lau et al. (2018): $Q_o \sim 0.24 \text{ MeV}$ per baryon for extreme rp-process ashes and $Q_o \sim 0.29 \text{ MeV}$ for superburst and KEPLER ashes (the values are read out from their figures for the density corresponding to $P_{nd}^{(cat)}$ for different ashes). The difference is likely related to the fact, that these authors include excited states in their simulations and treated separately electron captures and neutron emission processes. However, as discussed in Shchepochin & Chugunov (2019), for some transitions (for example, for beta-captures by ^{56}Fe) the theoretical model applied in Lau et al. (2018) overestimates the energy of the first excited state, leading to unrealistic increase of the heating associated with this reaction. We checked that for superburst ashes one of the sources of the discrepancy between our results and those of Lau et al. (2018) is the delayed beta-captures by ^{56}Fe in Lau et al. (2018). We also checked that, generally, the composition profiles and the reaction network pathways predicted by our simplified reaction network for FRDM92 mass model are in a reasonable agreement with the

results shown in Lau et al. (2018), which are based on the same mass model. In particular, the impurity parameter profile agrees very well with that calculated by Lau et al. (2018) (see Fig. A3 in Appendix A). This confirms the applicability of our model as a tool for simplified modelling of the reaction network in the crust.

In Appendix A we present results of our detailed calculations of the average charge and impurity parameter profiles for all the considered models. These data are required for modelling the thermal evolution of NS crust. It should be noted that the average charge profile only weakly depends on the theoretical mass model (see Fig. A2). In contrast, the impurity parameter appears to be rather sensitive to the employed mass model at sufficiently large pressures near the outer/inner crust interface (Fig. A1).

3.2 Deep crustal heating in the nHD approach

Let us start with the accurate definition of the total deep crustal heat release Q following GC21. GC21 introduces the redshifted heat release Q^∞ (as seen by a distant observer) which, strictly speaking, depends on the NS mass and EOS in the core. However, for nHD models this dependence can be removed if we define the ‘local’ quantity Q according to the formula: $Q = Q^\infty e^{-\nu_{oi}/2}$, where $e^{\nu_{oi}/2}$ is the redshift factor at the oi interface (see equation (4) in GC21). The factor $e^{\nu_{oi}/2}$ almost coincides with the redshift factor at the surface. Assuming, for instance, an NS with BSk24 EOS in the core and crust, the latter varies from 0.86 to 0.76 for NSs in the mass range $1.1M_\odot - 1.8M_\odot$. The parameter Q will be referred to as the total deep crustal heat release in what follows. As shown in GC21, in the regime of a FA crust Q can be parametrized by the pressure P_{oi} .

According to GC21, Q^∞ can be presented as a sum of three redshifted heat releases: (a) in the outer crust, $Q_o^\infty \approx Q_o e^{\nu_{oi}/2}$ (accurate calculation of Q_o^∞ should take into account variation of the redshift factor in the outer crust, but it leads to negligible effect, see section II in the supplementary material of GC21); (b) Q_{oi}^∞ at the oi interface; and (c) Q_i^∞ in the inner crust (including the heat released as a result of the instability leading to disintegration of nuclei, see Gusakov & Chugunov 2020; GC21). Let us denote $Q_{\text{inner}}^\infty = Q_{oi}^\infty + Q_i^\infty$ and apply a simple expression for this quantity, derived in section III of the supplementary material in GC21:

$$Q_{\text{inner}}^\infty = e^{\nu_{oi}/2} [\mu_b(P_{oi}) - m_n]. \quad (1)$$

Here $\mu_b(P_{oi})$ is the baryon chemical potential at the bottom of the outer crust and m_n is the neutron mass. Equation (1) can be interpreted as a heat release in an abstract ‘reaction’ that summarizes all the reactions at the outer-inner crust interface and in the inner crust, and eventually converts all the upcoming nuclei (with the redshifted baryon chemical potential $\mu_b(P_{oi})e^{\nu_{oi}/2}$) into baryons in the core (thanks to the nHD condition, the redshifted baryon chemical potential in the core equals $m_n e^{\nu_{oi}/2}$).

The composition at the bottom of the outer crust is calculated in Section 3.1, making μ_b a known function of P_{oi} and thus allowing us to apply Eq. (1). The results are shown in Fig. 2, where we present $Q_{\text{inner}} = Q_{\text{inner}}^\infty e^{-\nu_{oi}/2}$ and $Q = Q_o + Q_{\text{inner}}$ as functions of P_{oi} for all the considered mass models and ash compositions. In the bottom panel, which

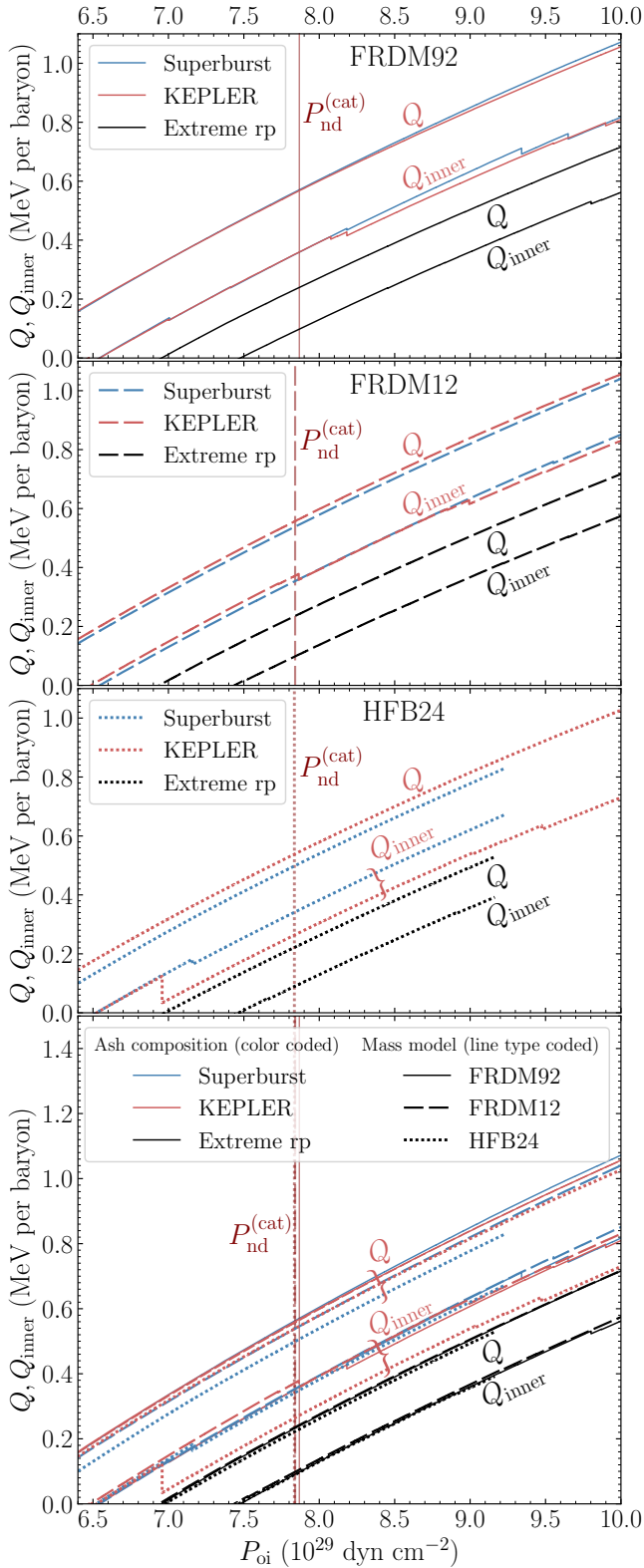


Figure 2. Q and Q_{inner} vs outer-inner crust transition pressure P_{oi} . As in Fig. 1, the three upper panels represent results for the respective mass model, while the bottom panel combines all the results in one plot. Ash compositions are colour coded (superburst – blue; KEPLER – red; extreme rp – black); the mass models are line type coded (FRDM92 – solid; FRDM12 – dashed; HFB24 – dotted lines). Vertical lines indicate pressure at the outer-inner crust interface for the cold catalysed crust (line type corresponds to the mass model).
MNRAS **000**, 1–10 (2021)

combines all the results in one plot, the groups of lines, corresponding to Q_{inner} and Q are marked by braces. For HFB24 mass model dotted lines are ended at $P = P_{\text{nd}}^{(\text{acc})}$; for other mass models $P_{\text{nd}}^{(\text{acc})}$ lies outside the plot.

One sees that all ashes lead to approximately linear $Q_{\text{inner}}(P_{\text{oi}})$ dependence. The only exception is KEPLER ashes in HFB24 model, for which Q_{inner} drops by ≈ 0.09 MeV per baryon at $P \approx 7 \times 10^{29}$ dyn cm $^{-2}$. The drop is associated with the electron captures with simultaneous emission of neutrons for ^{32}Ne at such P . This process converts ^{32}Ne into ^{28}O , which undergoes pycnonuclear fusion, leading to formation of ^{52}S and free neutrons (the neutrons are finally absorbed by other nuclei in the same layer). For FRDM92 and FRDM12 this process is not energetically favourable.

Note that, in contrast to the function $Q_{\text{inner}}(P_{\text{oi}})$, the Q -line in Fig. 2 always stays continuous. It may seem strange at first glance, but it is a typical feature: drops of $Q_{\text{inner}}(P_{\text{oi}})$ are associated with localized reactions in the outer crust, which release energy and lead to jumps of $Q_{\text{o}}(P_{\text{oi}})$. As a result, the total energy release Q is a smooth function of P_{oi} . The continuity of $Q(P_{\text{oi}})$ also follows directly from the equation (4) of GC21.

For the extreme rp-process ashes, Q_{inner} weakly depends on the nuclear mass model in the outer crust, being smaller than for the superburst and KEPLER ashes by ~ 0.3 MeV per baryon for the same P_{oi} . This difference is related to the higher mass number of nuclei in extreme rp-process ashes, which makes the corresponding nuclear composition at the bottom of the outer crust closer to the ground state. In particular, the ground state element at the outer-inner crust interface for FRDM92 and FRDM12 models is ^{118}Kr ($Z = 36$), while for HFB24 model it is ^{124}Sr ($Z = 38$; note that for other HFB models the mass number can be a bit different, see Chamel et al. 2015). In turn, for extreme rp-process ashes the most abundant nuclide at $P_{\text{oi}} = P_{\text{nd}}^{(\text{cat})}$ is ^{104}Ge ($Z = 32$) for all the considered mass models. This is in sharp contrast with the superburst and KEPLER ashes, for which the most abundant elements at the oi-interface have $Z \approx 18-20$ and $A \approx 60$ (see Fig. A2). Very different nuclear compositions at the oi-interface predicted by different ash models should strongly affect the overall composition of the inner crust, which is crucial for the determination of P_{oi} in the regime of FA crust (see GC21). We come to conclusion that the pressure P_{oi} will likely depend on the composition of ashes.

Similarly to GC21, we set a lower bound on the pressure P_{oi} by requiring $Q_{\text{inner}} > 0$. It gives $P_{\text{oi}} > 6.5 \times 10^{29}$ dyn cm $^{-2}$ for superburst and KEPLER ashes and $P_{\text{oi}} > 7.4 \times 10^{29}$ dyn cm $^{-2}$ for extreme rp-process ash. According to Fig. 2, these constraints correspond to $Q > 0.13 - 0.2$ MeV per baryon. This lower bound is an order of magnitude smaller than in the traditional approach and, probably, is not very restrictive (too small). We expect that a much more interesting lower bound on P_{oi} will be obtained by calculating the heat release at the oi-interface and in the shallow layer of the inner crust (where the theoretical atomic mass tables still can be trusted), and requiring that the remaining heat released in the deeper layers of the inner crust to be non-negative. We plan to perform such an analysis in our subsequent publication.

In GC21 we suggest that the catalyzed pressure $P_{\text{nd}}^{(\text{cat})}$ can serve as a conservative estimate for the upper bound on P_{oi} .

This conclusion is based on the results of detailed calculations of the inner crust composition performed within the CLD+sh model of Carreau et al. (2020) for pure ^{56}Fe nuclear ashes. Strictly speaking, applicability of this bound for other ash compositions should be checked, especially for extreme rp-process ash enriched by heavy nuclei. Anyhow, the respective values of the heating corresponding to $P_{\text{oi}} = P_{\text{nd}}^{(\text{cat})}$ can be easily read out from Fig. 2: $Q \sim 0.54$ MeV per baryon for superburst and KEPLER ashes and $Q \sim 0.24$ MeV per baryon for extreme rp-process ashes (cf. the value $1.5 - 2.0$ MeV per baryon obtained within the traditional approach).

4 SUMMARY

We apply the multi-component simplified reaction network to find the heat release Q_o and composition (in particular, the impurity parameter, Q_{imp} , and average charge, $\langle Z \rangle$) in the outer crust of accreting NS for different compositions of thermonuclear burning ashes (superburst, KEPLER, and extreme rp-process ashes). Calculations are made for the three theoretical atomic mass tables (FRDM92, FRDM12, and HFB24) to check the sensitivity of the results to the chosen nuclear mass model (note, however, that for nuclei with experimentally measured masses AME20 is applied).

We find, first of all, that the average charge profile in the outer crust is rather insensitive to the applied mass model (Fig. A2). This is in contrast to the strong model dependence of the heat release (Figs. 1, B2) and impurity parameter profiles (Fig. A1). It is notable that the latter parameter, obtained in our simplified reaction network, agrees well with Q_{imp} calculated by Lau et al. (2018) if the same mass model (FRDM92) is applied (Fig. A3). The fact that the heat release Q_o and impurity parameter Q_{imp} are sensitive to the employed theoretical mass model suggests that, currently, an uncertainty in determination of these quantities in the outer crust is rather dominated by the uncertainties in the mass models, than by the details of the reaction kinetics.

Having at hand Q_o , we determine the total deep crustal heat release, Q , and the heat release in the inner crust (including the outer-inner crust interface contribution), Q_{inner} , in the regime of a fully accreted crust following the thermodynamically consistent approach developed in GC21.

Our results for Q , Q_o and Q_{inner} are parametrized by the pressure P_{oi} at the outer-inner crust interface (Figs. 1, 2). As argued in GC21, accurate calculation of P_{oi} depends sensitively on the inner crust EOS, which has not yet been analysed within the nHD approach for complex ash compositions. In this work we, therefore, treat P_{oi} as a free parameter. We constrain P_{oi} from below by the requirement $Q_{\text{inner}} > 0$, which gives: $P_{\text{oi}} > 6.5 \times 10^{29}$ dyn cm $^{-2}$ for superburst and KEPLER ashes and $P_{\text{oi}} > 7.4 \times 10^{29}$ dyn cm $^{-2}$ for extreme rp-process ashes, implying $Q > 0.13 - 0.2$ MeV per baryon. It is much more complicated to constrain P_{oi} from above (see Section 3.2).

For the same P_{oi} superburst and KEPLER ashes lead to a larger heating than the extreme rp-process ash (the difference is ~ 0.3 MeV per baryon); however, we warn the reader, that the actual P_{oi} likely depends on the ash composition and this can (partially) compensate the difference (for instance, such partial compensation takes place for the lower bounds on Q quoted above).

An important advantage of our approach, based on GC21, is that it encodes all uncertain physics of deep inner crust layers in just one parameter, P_{oi} . In our calculations, we deal mostly with the masses of neutron-rich isotopes before the neutron-drip line. There is great progress in experimental measurements of the masses of such nuclei (e.g., Meisel et al. 2020) and new experiments are planned (Kim 2020; Meisel 2020). This gives us hope that the profiles $Q(P_{\text{oi}})$ and $Q_{\text{inner}}(P_{\text{oi}})$ will become more certain in the not-too-distant future (even nowadays the uncertainty associated with the theoretical mass models is rather modest, see Fig. 2). This opens up an attractive possibility to constrain P_{oi} by comparing observations of crustal coolers with the theoretical modelling of their thermal evolution.

In a subsequent publication, we plan to continue and extend this work by analysing the shallow layers of the inner crust and calculating the heating profile and nuclear composition there. Apart from the fact that this information is vitally important for modelling the thermal evolution of transiently accreting NSs, we expect that it will also allow us to tighten a lower bound on P_{oi} by imposing the condition that the heat release in the remaining part of the inner crust should be positive.

ACKNOWLEDGEMENTS

The work of N. N. Shchepochin was supported by the Foundation for the Advancement of Theoretical Physics and Mathematics “BASIS” (grant #20-1-5-79-1). The work of M. E. Gusakov was supported by RFBR [Grant No. 19-52-12013].

DATA AVAILABILITY

Data can be provided by the authors upon a reasonable request.

REFERENCES

- Afanasjev A. V., Beard M., Chugunov A. I., Wiescher M., Yakovlev D. G., 2012, *Phys. Rev. C*, **85**, 054615
- Beznogov M. V., Yakovlev D. G., 2015, *MNRAS*, **452**, 540
- Brack M., Guet C., Håkansson H. B., 1985, *Phys. Rep.*, **123**, 275
- Brown E. F., Cumming A., 2009, *Astrophys. J.*, **698**, 1020
- Brown E. F., Bildsten L., Rutledge R. E., 1998, *ApJ*, **504**, L95
- Brown E. F., Cumming A., Fattoyev F. J., Horowitz C. J., Page D., Reddy S., 2018, *Phys. Rev. Lett.*, **120**, 182701
- Cackett E. M., Brown E. F., Cumming A., Degenaar N., Miller J. M., Wijnands R., 2010, *ApJ*, **722**, L137
- Carreau T., Gulminelli F., Chamel N., Fantina A. F., Pearson J. M., 2020, *A&A*, **635**, A84
- Chamel N., Fantina A. F., Zdunik J. L., Haensel P., 2015, *Phys. Rev. C*, **91**, 055803
- Chamel N., Fantina A. F., Zdunik J. L., Haensel P., 2020, *Phys. Rev. C*, **102**, 015804
- Chugunov A. I., 2019, *MNRAS*, **483**, L47
- Chugunov A. I., Shchepochin N. N., 2020, *MNRAS*, **495**, L32
- Cumming A., Macbeth J., in ’t Zand J. J. M., Page D., 2006, *ApJ*, **646**, 429
- Cybart R. H., Amthor A. M., Heger A., Johnson E., Keek L., Meisel Z., Schatz H., Smith K., 2016, *ApJ*, **830**, 55
- Degenaar N., Wijnands R., Miller J. M., 2013, *ApJ*, **767**, L31

- Fantina A. F., Zdunik J. L., Chamel N., Pearson J. M., Haensel P., Goriely S., 2018, *A&A*, **620**, A105
- Fortin M., Taranto G., Burgio G. F., Haensel P., Schulze H. J., Zdunik J. L., 2018, *MNRAS*, **475**, 5010
- Fortin M., Raduta A. R., Avancini S., Providencia C., 2021, arXiv e-prints, p. [arXiv:2102.07565](#)
- Goriely S., Chamel N., Pearson J. M., 2010, *Phys. Rev. C*, **82**, 035804
- Goriely S., Chamel N., Pearson J. M., 2013, *Phys. Rev. C*, **88**, 024308
- Gupta S., Brown E. F., Schatz H., Möller P., Kratz K.-L., 2007, *ApJ*, **662**, 1188
- Gupta S. S., Kawano T., Möller P., 2008, *Physical Review Letters*, **101**, 231101
- Gusakov M. E., Chugunov A. I., 2020, *Phys. Rev. Lett.*, **124**, 191101
- Gusakov M. E., Chugunov A. I., 2021, *Phys. Rev. D*, **103**, L101301
- Haensel P., Zdunik J. L., 1990a, *A&A*, **227**, 431
- Haensel P., Zdunik J. L., 1990b, *A&A*, **229**, 117
- Haensel P., Zdunik J. L., 2003, *A&A*, **404**, L33
- Haensel P., Zdunik J. L., 2008, *A&A*, **480**, 459
- Haensel P., Potekhin A., Yakovlev D., 2007, *Neutron Stars 1: Equation of State and Structure. Astrophysics and Space Science Library*, Springer-Verlag, Berlin
- Han S., Steiner A. W., 2017, *Phys. Rev. C*, **96**, 035802
- Heinke C. O., Jonker P. G., Wijnands R., Taam R. E., 2007, *ApJ*, **660**, 1424
- Heinke C. O., Jonker P. G., Wijnands R., Deloye C. J., Taam R. E., 2009, *ApJ*, **691**, 1035
- Johnston Z., 2020, arXiv e-prints, p. [arXiv:2004.00012](#)
- Keek L., Heger A., 2011, *ApJ*, **743**, 189
- Kim Y. J., 2020, *Nuclear Instruments and Methods in Physics Research B*, **463**, 408
- Lau R., et al., 2018, *ApJ*, **859**, 62
- Levenfish K. P., Haensel P., 2007, *Astrophys. Space Sci.*, **308**, 457
- Lunney D., Pearson J. M., Thibault C., 2003, *Reviews of Modern Physics*, **75**, 1021
- Mackie F. D., Baym G., 1977, *Nuclear Phys. A*, **285**, 332
- Meisel Z., 2020, in *Journal of Physics Conference Series*. p. 012026, doi:[10.1088/1742-6596/1668/1/012026](#)
- Meisel Z., Deibel A., Keek L., Shternin P., Elfritz J., 2018, *Journal of Physics G Nuclear Physics*, **45**, 093001
- Meisel Z., et al., 2020, *Phys. Rev. C*, **101**, 052801
- Möller P., Nix J. R., Myers W. D., Swiatecki W. J., 1995, *Atomic Data and Nuclear Data Tables*, **59**, 185
- Möller P., Sierk A. J., Ichikawa T., Sagawa H., 2016, *Atomic Data and Nuclear Data Tables*, **109**, 1
- Page D., Reddy S., 2013, *Phys. Rev. Lett.*, **111**, 241102
- Parikh A. S., et al., 2019, *A&A*, **624**, A84
- Parikh A. S., Degenaar N., Hernández Santisteban J. V., Wijnands R., Psaradaki I., Costantini E., Modiano D., Miller J. M., 2021a, *MNRAS*, **501**, 1453
- Parikh A. S., Degenaar N., Hernández Santisteban J. V., Wijnands R., Psaradaki I., Costantini E., Modiano D., Miller J. M., 2021b, *Monthly Notices of the Royal Astronomical Society*, **502**, 2826
- Potekhin A. Y., Chabrier G., 2021, *A&A*, **645**, A102
- Potekhin A. Y., Chugunov A. I., Chabrier G., 2019, *A&A*, **629**, A88
- Rutledge R. E., Bildsten L., Brown E. F., Pavlov G. G., Zavlin V. E., Ushomirsky G., 2002, *The Astrophysical Journal*, **580**, 413
- Saakyan G. S., Avakyan R. M., 1972, *Astrophysics*, **8**, 70
- Sato K., 1979, *Progress of Theoretical Physics*, **62**, 957
- Schatz H., et al., 2001, *Nuclear Phys. A*, **688**, 150
- Shchechilin N. N., Chugunov A. I., 2019, *MNRAS*, p. 2428
- Shternin P. S., Yakovlev D. G., Haensel P., Potekhin A. Y., 2007, *Mon. Not. R. Astron. Soc.*, **382**, L43
- Steiner A. W., 2012, *Phys. Rev. C*, **85**, 055804
- Strutinsky V. M., 1967, *Nuclear Phys. A*, **95**, 420
- Wang M., Audi G., Kondev F. G., Huang W. J., Naimi S., Xu X., 2017, *Chinese Physics C*, **41**, 030003
- Wang M., Huang W. J., Kondev F. G., Audi G., Naimi S., 2021, *Chinese Physics C*, **45**, 030003
- Wijnands R., Degenaar N., Page D., 2013, *MNRAS*, **432**, 2366
- Wijnngaarden M. J. P., et al., 2020, *MNRAS*, **493**, 4936
- Xu, Y. Goriely, S. Jorissen, A. Chen, G. L. Arnould, M. 2013, *A&A*, **549**, A106
- Yakovlev D. G., Levenfish K. P., Haensel P., 2003, *A&A*, **407**, 265
- Yakovlev D. G., Levenfish K. P., Potekhin A. Y., Gnedin O. Y., Chabrier G., 2004, *Astron. Astrophys.*, **417**, 169
- Yakovlev D. G., Gasques L. R., Afanasjev A. V., Beard M., Wiescher M., 2006, *Phys. Rev. C*, **74**, 035803

APPENDIX A: IMPURITY PARAMETER AND AVERAGE CHARGE

For completeness, in Figs. A1 and A2 we present profiles of the average charge $\langle Z \rangle = \sum_i X_i Z_i$ and the impurity parameter $Q_{\text{imp}} = \sum_i X_i (Z_i - \langle Z \rangle)^2$, where X_i denotes the fractional number of ions of type i . These data can be useful for modelling the thermal evolution of accreting NSs.

It is interesting that the function $Q_{\text{imp}}(P_{\text{oi}})$ is sensitive to the employed mass model for sufficiently large pressures ($P_{\text{oi}} \gtrsim 6 \times 10^{29} \text{ dyn cm}^{-2}$; see bottom panel in Fig. A1). At the same time, $\langle Z \rangle$ -profile remains roughly the same for different mass models (see bottom panel in Fig. A2).

In Fig. A3 we compare profiles of Q_{imp} calculated within our reaction network (solid and dashed lines) with Q_{imp} presented by Lau et al. (2018) (dots; the corresponding data were read out from their figure 24). To plot Fig. A3, we adopt the same theoretical mass table FRDM92 as was used by Lau et al. (2018), but supplement it with AME16 (dashes) or AME20 (solid lines) experimental mass tables. One sees a very good agreement between all the three calculations. This means that the simplified reaction network developed in this work can be used for reliable calculations of the impurity parameter and average charge profiles in the outer crust.

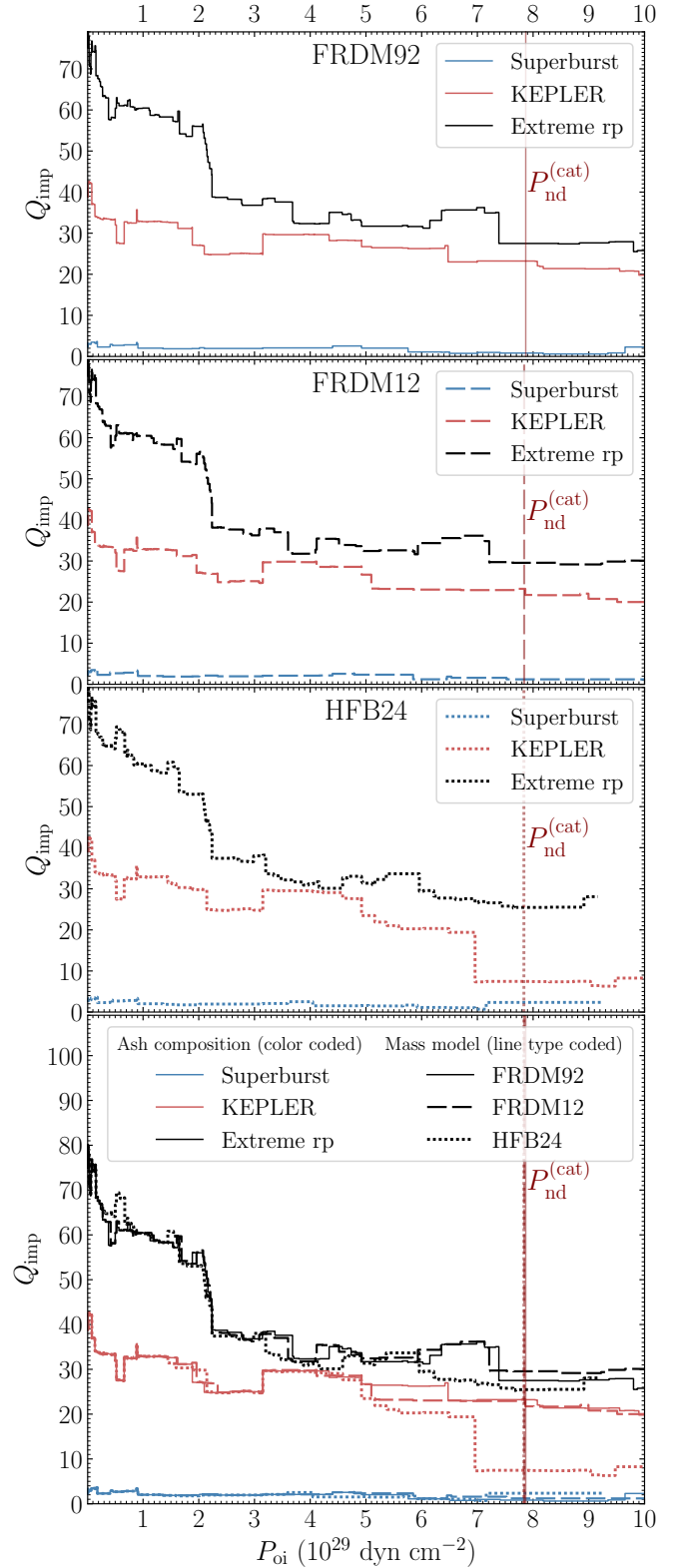


Figure A1. Q_{imp} vs P_{oi} for the three ash compositions considered in the paper. As in Fig. 1, the three upper panels represent results for the respective mass model, while the bottom panel combines all the results in one plot. Ash compositions are colour coded (superburst – blue; KEPLER – red; extreme rp – black); the mass models are line type coded (FRDM92 – solid; FRDM12 – dashed; HFB24 – dotted lines). Vertical lines indicate pressure at the outer-inner crust interface for the cold catalysed crust (line type corresponds to the mass model).

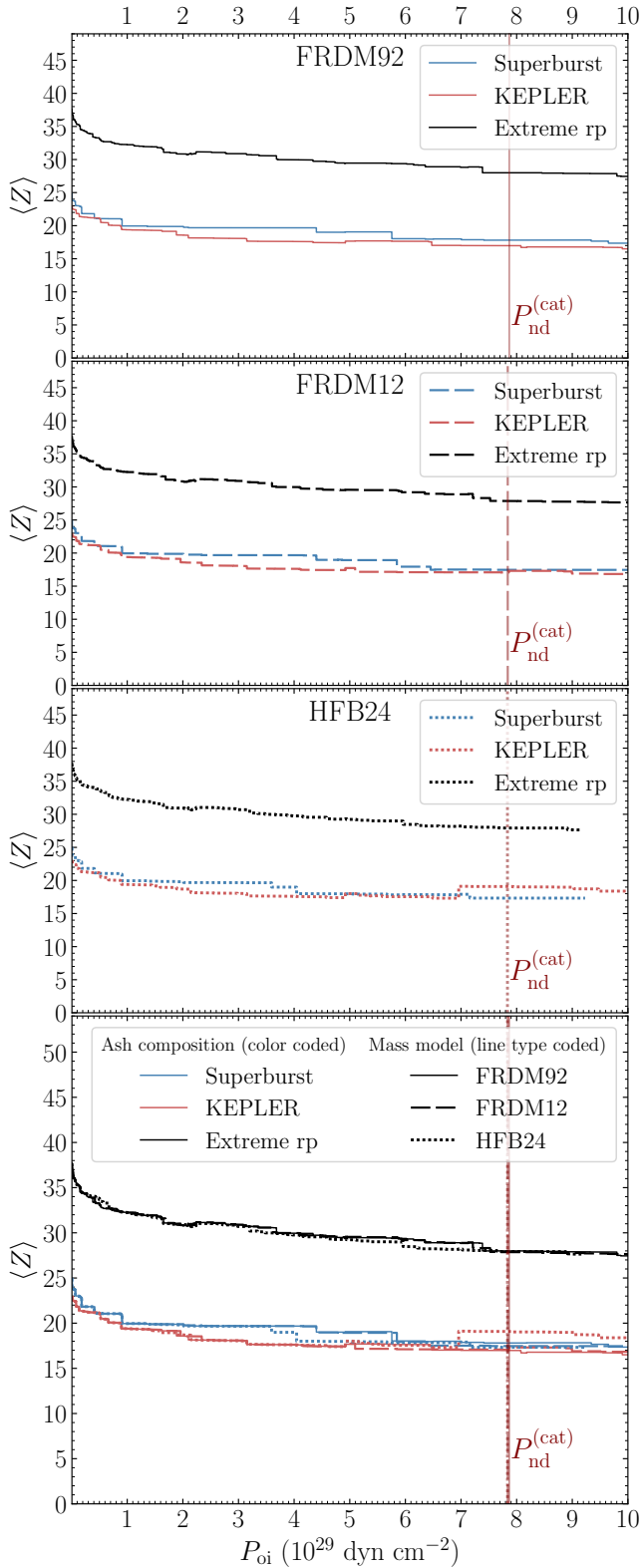


Figure A2. $\langle Z \rangle$ vs P_{oi} for the three ash compositions considered in the paper. The notations are the same as in Fig. A1.

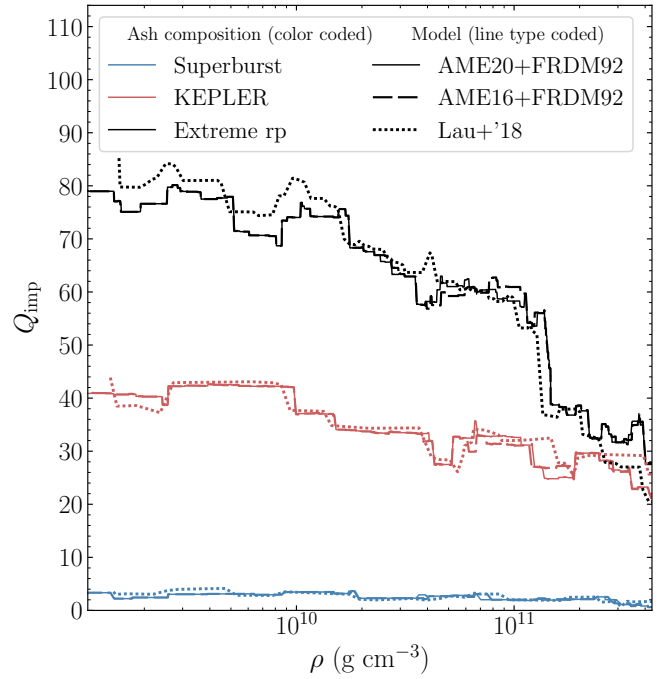


Figure A3. Comparison of the impurity parameter profile $Q_{imp}(\rho)$ in the outer crust calculated within the simplified reaction network (solid and dashed lines), with the results by Lau et al. (2018) (dotted lines). Ash compositions are color coded (superburst – blue; KEPLER – red; extreme rp – black); the models are line type coded (AME20+FRDM92 – solid; AME16+FRDM92 – dashed; Lau+'18 – dotted lines).

APPENDIX B: COMPARISON OF THE EMPLOYED THEORETICAL MASS MODELS AND IMPORTANCE OF THE PROGRESS IN EXPERIMENTAL NUCLEAR MASS MEASUREMENTS

Figure B1 compares the theoretical mass models employed in this work. One can notice substantial uncertainties in the mass values of the neutron-rich nuclei, used in our calculations. This uncertainty increases with increase of the neutron excess and distance from nuclei with experimentally measured masses (indicated by open circles, small dots and filled circles; see caption to the figure).

Recently, the experimental mass table AME16 has been replaced by the new one, AME20. To demonstrate importance of this update, below we present analogues of Figs. 1 and 2, calculated using AME16 instead of AME20 (see Figs. B2 and B3). We confronted these figures and found noticeable changes in the energy release profile and outer crust composition for AME20 in comparison to AME16 table (however, qualitatively, the results remain unchanged). In particular, the difference between the curves in the figures corresponding to different theoretical mass models is slightly reduced for AME20, emphasizing the role of new experimental nuclear mass measurements for astrophysical applications.

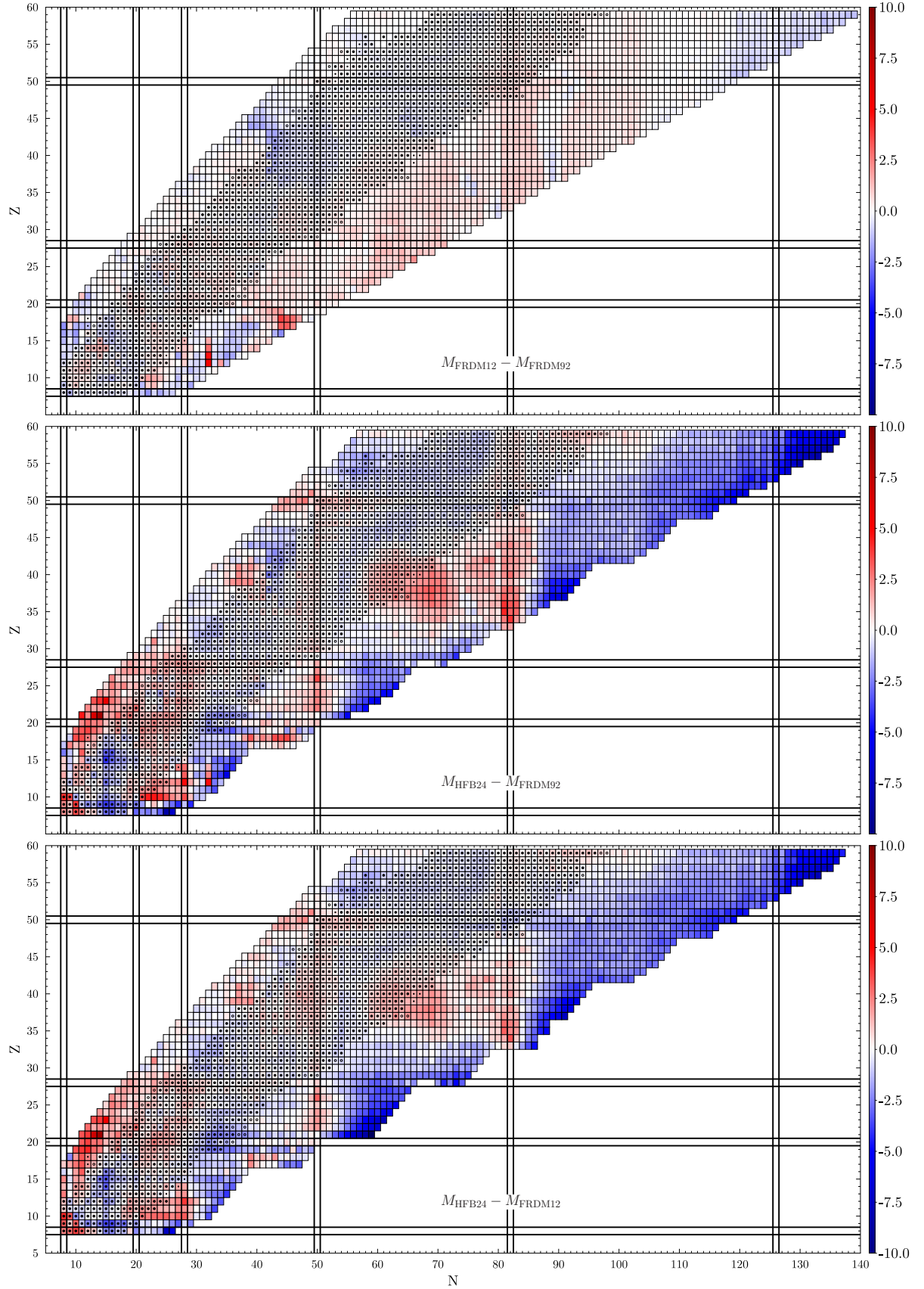


Figure B1. Mass differences (in MeV) for theoretical mass models employed in this work. Magic numbers are shown by pairs of thick solid lines. Nuclei with known experimental masses are indicated by symbols in the centre of respective square. Open circles, small dots, and filled circles are for nuclei that are presented only in AME20, only in AME16, and in both AME20 and AME16 tables, respectively.

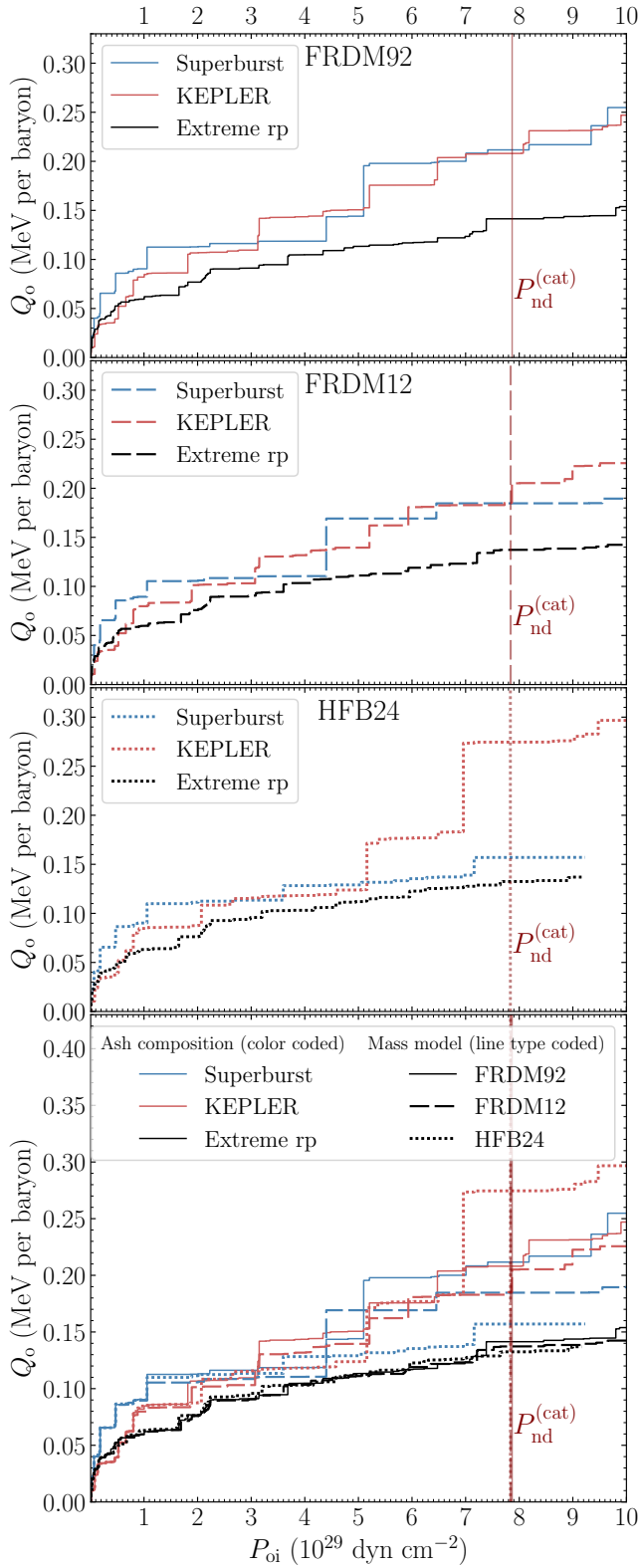


Figure B2. Analogue of the figure 1, but with AME16 applied as the experimental atomic mass table.

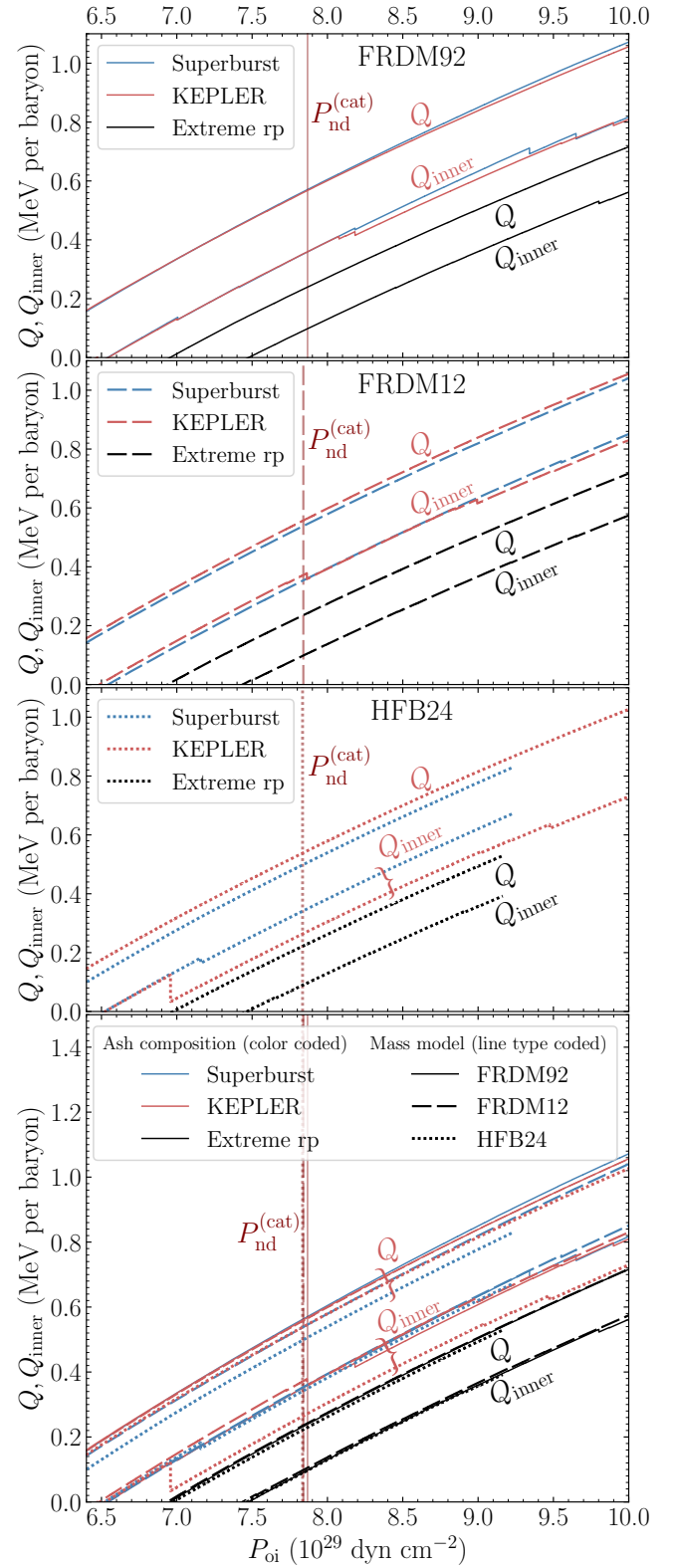


Figure B3. Analogue of the figure 2, but with AME16 applied as the experimental atomic mass table.